AGU PUBLICATIONS

JGR

Journal of Geophysical Research: Atmospheres

RESEARCH ARTICLE
10.1002/2017JD026615

Special Section:
Atmospheric Gravity Wave Science in the Polar Regions and First Results from ANGWIN

Observations and fine-scale model simulations of gravity waves over Davis, East Antarctica (69°S, 78°E)

S. P. Alexander[1,2], A. Orr[3], S. Webster[4], and D. J. Murphy[1,2]

[1]Australian Antarctic Division, Hobart, Tasmania, Australia, [2]Antarctic Climate and Ecosystems Cooperative Research Centre, Hobart, Tasmania, Australia, [3]British Antarctic Survey, Cambridge, UK, [4]Met Office, Exeter, UK

Abstract Large vertical velocities were observed throughout the troposphere at Davis, East Antarctica, on 18 February 2014 by a VHF wind-profiling radar. Simulations using the Met Office Unified Model at 2.2, 0.5, and 0.1 km horizontal grid spacing were able to broadly capture the location, timing, and magnitude of the observed velocities, as well as reveal that they are due to small-scale orographic gravity waves resulting from the interaction between the coastal topography and strong easterly winds associated with a synoptic-scale cyclone situated to the north. The simulations indicated that the gravity waves are responsible for (i) temperature fluctuations which coincided with satellite-observed cloud variations in the vicinity of Davis, suggesting that they have a crucial role in the formation of cirrus clouds, and (ii) large vertical momentum fluxes in the troposphere. The waves are prevented from propagating into the stratosphere by the background winds turning from near-surface easterlies to lower stratospheric northerlies. As well as illuminating and quantifying the role that weather systems have in producing orographic gravity waves along the East Antarctic coastline, studies such as this should be exploited to improve the representation of key localized atmospheric processes in global climate models.

Key Points:
- Large vertical velocities observed by Davis radar are simulated by the UM
- Simulations indicate synoptic winds, and coastal topography interact to form OGW
- Temperature fluctuations induced by OGW influence local cloud presence

Correspondence to:
S. P. Alexander,
Simon.Alexander@aad.gov.au

Citation:
Alexander, S. P., A. Orr, S. Webster, and D. J. Murphy (2017), Observations and fine-scale model simulations of gravity waves over Davis, East Antarctica (69°S, 78°E), *J. Geophys. Res. Atmos.*, *122*, 7355–7370, doi:10.1002/2017JD026615.

Received 8 FEB 2017
Accepted 20 JUN 2017
Accepted article online 29 JUN 2017
Published online 21 JUL 2017

1. Introduction

The climatological winds along the East Antarctic coastline are influenced by both transient synoptic-scale depressions located to the north of the continent and katabatic flows spilling down from the high, cold interior. The strongest wind events mostly occur along the coast at times when katabatic flows are enhanced by synoptic winds associated with the passage of these depressions [*Turner et al.*, 2009; *Orr et al.*, 2014]. These synoptic winds are often blocked by the elevated coastal terrain which typifies East Antarctica, resulting in the formation of strong coast-parallel winds known as barrier jets [*Steinhoff et al.*, 2008; *Nigro et al.*, 2012]. The interaction between winds and abrupt variations in topography, surface roughness, and temperature (e.g., at the interface between sea and land) can also create localized variations in the wind field such as coastal and detached jets, which can only be represented by high-resolution models [*Hunt et al.*, 2004; *Owinoh et al.*, 2005; *Orr et al.*, 2005; *Turner et al.*, 2009].

Orographic gravity waves in East Antarctica are produced by synoptic winds or katabatic winds interacting with mountains or coastal ice ridgelines and generally occur on small spatial scales ranging from a few to hundreds of kilometers [*Watanabe et al.*, 2006; *Valkonen et al.*, 2010; *Orr et al.*, 2014; *Alexander and Murphy*, 2015; *Plougonven et al.*, 2015]. The transient cyclones located offshore are sources of nonorographic gravity waves [*Plougonven et al.*, 2015; *Alexander et al.*, 2016], as are jet front readjustments of unbalanced flows [*Guest et al.*, 2000; *Hendricks et al.*, 2014; *Alexander et al.*, 2016]. These orographic gravity waves propagate energy leeward of the topographical forcing feature when their wave number vectors are not parallel to the background flow [*Sato et al.*, 2012].

High-frequency gravity wave activity can be quantified by analyzing wind velocities obtained with very high frequency (VHF) radars. These VHF radars provide profiles of wind velocities in the lower atmosphere at high temporal resolution (on the order of minutes for a complete set of zonal u, meridional v, and vertical w velocity profiles over ~2–15 km altitudes). An analysis of 2 years of data collected at Davis, Antarctica (69°S, 78°E) revealed a seasonal cycle of lower tropospheric gravity wave activity, peaking in winter [*Alexander and Murphy*, 2015]. Increased gravity wave activity is related closely to the passage of offshore synoptic-scale depressions, which direct strong northeasterly flow along the coastline and form orographic gravity waves via interaction with coastal topography [*Alexander and Murphy*, 2015]. Vertical velocities measured by a radar at Wasa

(73°S, 13°W) were used alongside output from a high-resolution model to examine summertime case studies of flow over small-scale topography [*Valkonen et al.*, 2010; *Arnault and Kirkwood*, 2012]. A winter case study of large *w* observed in radar data at Syowa (69°S, 40°E) coincided with a deep depression centered to the north which directed strong winds parallel to the coastline [*Tomikawa et al.*, 2015].

The region of East Antarctica around Davis is a hot spot for orographic gravity wave activity [*Hoffmann et al.*, 2013]. One of the key effects of vertically propagating orographic gravity waves is to transport horizontal momentum of the mean flow from their source regions up to where they are either dissipated or absorbed [*Smith*, 1979]. The resulting deposition of momentum is important for driving the large-scale circulation in the troposphere and lower stratosphere. The effects of subgrid-scale orographic gravity waves are parametrized in coarse-grid global atmospheric models. Output from high-resolution simulations that are better able to resolve gravity waves and hence quantify the vertical distribution of momentum flux are used to improve deficiencies in these schemes [e.g., *Vosper*, 2015]. Another key effect of vertically propagating orographic gravity waves is the formation of clouds, such as cirrus in the upper troposphere [*Ludlam*, 1952; *Kärcher and Ström*, 2003; *Dean et al.*, 2005] and polar stratospheric clouds in winter [*Alexander et al.*, 2011]. Orographic cirrus clouds can have a strong influence on the surface radiative budget, as well as on the distribution of water vapor [*Stephens*, 2002]. The small-scale temperature fluctuations that can trigger such clouds also require parametrization in global models, as well as the use of high-resolution simulations to improve them [*Orr et al.*, 2015].

Antarctic stations are isolated and rely heavily on aircraft for logistics and science operations. Hence, they require accurate forecasts, especially during the summer operational season. The UK Met Office Unified Model (UM) is a forecast model which, although mainly developed and evaluated at midlatitudes, has been increasingly used for the polar regions [*Orr et al.*, 2004; *Petersen et al.*, 2009; *Turner et al.*, 2009]. Recently, UM simulations at 1.5 km horizontal grid spacing were used to investigate a strong wind event at Mawson station in East Antarctica [*Orr et al.*, 2014]. Assessing the UM's dynamical performance throughout the East Antarctic troposphere would further aid identification of model deficiencies and aspects which require improvement.

In this study, we will run a high-resolution nested simulation using the UM to understand in the regional context a summertime case study of large gravity wave activity observed in the troposphere and lower stratosphere by the VHF radar at Davis station on 18 February 2014. A summertime case study provides the opportunity to evaluate the UM around Davis during the summer Antarctic operational season. This is the first case study of a summertime Antarctic strong wind event which leads to orographic gravity wave production along the coastline. Analysis of the UM in the region around Davis will provide spatial information on the forcing mechanisms and propagation of the waves observed by the radar and their role in the formation of ice clouds and transport of momentum.

2. Data and Modeling

2.1. Observations

The Davis VHF wind-profiling radar is a 55 MHz system located at sea level. It was reconfigured and upgraded in January 2014 from the original hybrid Doppler-full correlation analysis system to a pure Doppler system, with the objective of increasing the height coverage and accuracy of winds from the midtroposphere up to the lower stratosphere. Radial velocities are obtained in the vertical, north, and east directions (with the off-vertical beams pointing at a 14° zenith angle), cycling every 6 min. The vertical range resolution is 500 m, and wind velocities are obtained from 1.5 km above sea level up to the lower stratosphere. The winds derived from the radar's radial velocity measurements are successfully validated against colocated radiosonde observations (see Appendix A). Wind profiles from 1.5 km to the lower stratosphere are formed by implementing the outlier removal technique of *Dolman and Reid* [2014].

2.2. Modeling

The UM is a grid point model based on nonhydrostatic dynamics [*Davies et al.*, 2005]. The simulations are based on the atmosphere-only nested suite configuration of the UM (version 10.2). They use a N512 global version of the model (1024 × 769 grid points) to provide boundary conditions for three one-way nested domains centered over Davis (shown in Figure 1). The outer two domains have grid spacing of 2.2 and 0.5 km (with 600 × 600 and 900 × 900 grid points, respectively), with orography based on the GLOBE (Global Land One-kilometer Base Elevation) data set. The inner domain is at 100 m (with 1200 × 1200 grid points) and covers the entire Davis local area, with orography based on the ASTER (Advanced Spaceborne Thermal Emission

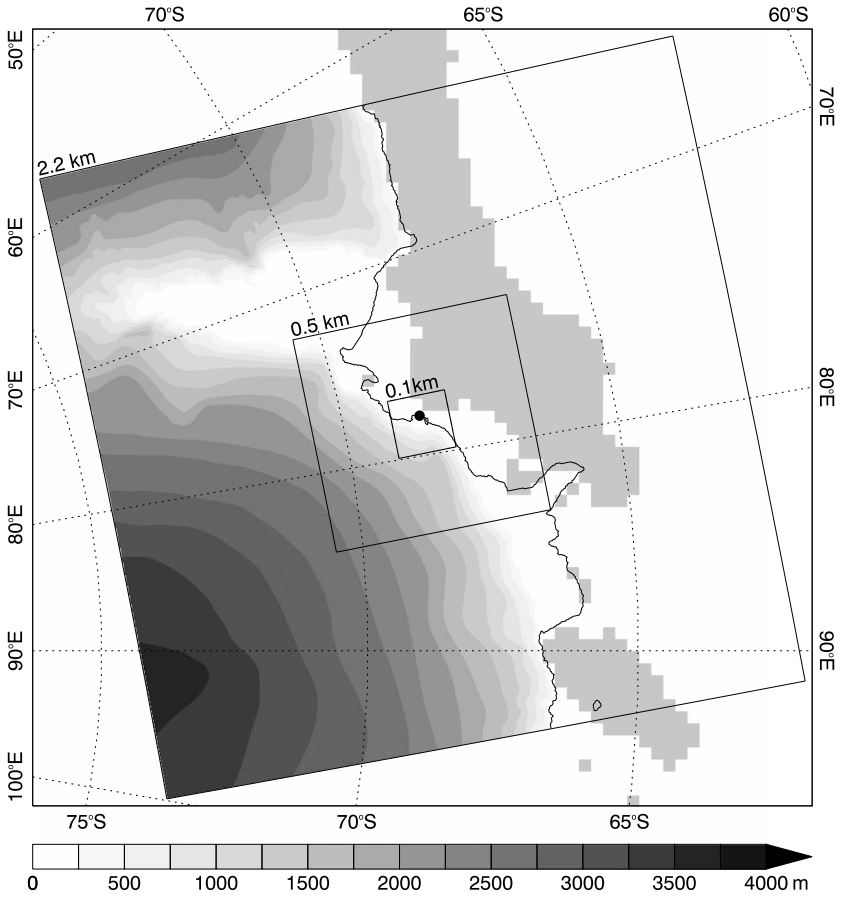

Figure 1. Domains of the three UM simulations, labeled with their resolutions. The location of Davis is indicated with a black dot. Model orography and the land/sea mask edge is shown at 2.2 km resolution. The pale grey boxes offshore are the individual 25 km pixels for which sea ice concentration exceeded the 15% level on 18 February 2014. Sea ice data are from the daily OSTIA.

and Reflection Radiometer) data set at 100 m resolution, which enables a better representation of features such as the coastal margins. The nested domains use a rotated latitude-longitude grid to achieve uniform grid spacing. In the vertical, 70 hybrid-height levels are used between the surface and the model top of 40 km. The model includes a comprehensive set of parameterizations which are similar to that described by *Orr et al.* [2014]. The global model was initialized at 0000 UTC on 17 February 2014 using Met Office operational analysis. Daily Operational Sea Surface Temperature and Sea Ice Analysis (OSTIA) data were additionally used to initialize the sea ice state and sea surface temperature of the nested domains. The simulations were run forward for 48 h.

3. Results

3.1. Synoptic Situation

The NOAA 15 advanced very high resolution radiometer (AVHRR) satellite image from 1146 UT, 18 February 2014 is shown in Figure 2 along with the geopotential height and horizontal wind field from the ERA-Interim reanalysis [*Dee et al.*, 2011] on the 500 hPa pressure level. A deep depression is centered north of Davis which directs northeasterly winds along the Antarctic coastline toward Davis. Substantial amounts of low-level cloud (indicated by the grey colors) spiral in to the depression's center (at 63°S, 78°E) on its southern and western sides. Extensive cloud cover is visible along the coastline.

3.2. Davis Radar Observations

The 6 min resolution time series of w at each altitude observed by the radar are shown in Figure 3 over the 3 day interval of 17–19 February 2014. The lapse rate tropopause altitudes derived from colocated radiosonde data are indicated. The radar tropopause altitude is calculated every 2 h and is defined as the level

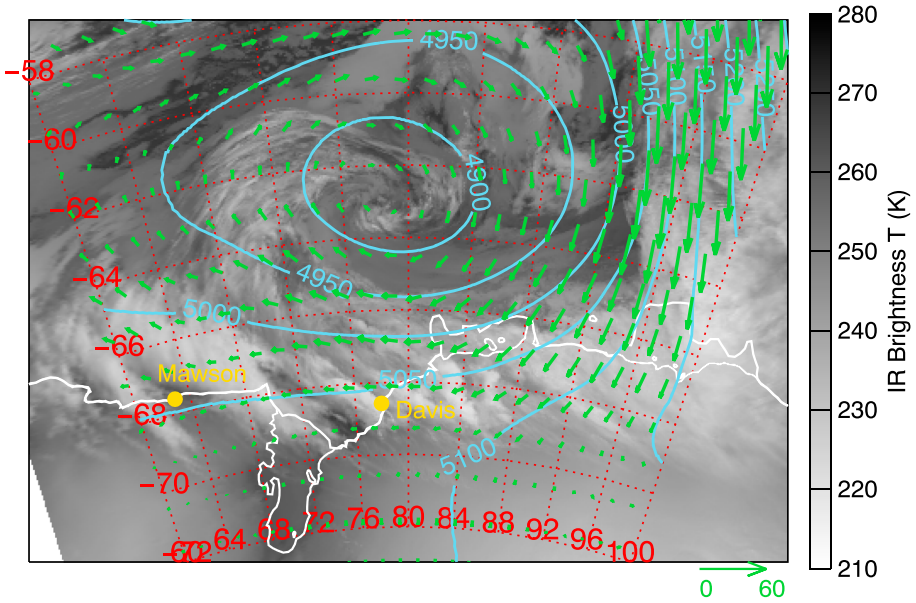

Figure 2. NOAA 15 satellite AVHRR Channel 4 infrared brightness temperature at 1146 UT 18 February along with the ERA-Interim geopotential height at 500 hPa (blue contours, units of meter) and the 500 hPa horizontal wind field (green vectors, scale at bottom with units m s^{-1}) at 1200 UT the same day. Davis and Mawson stations are indicated by the yellow filled circles.

of the maximum vertical gradient of radar echo return power [*Gage and Green*, 1979]. It corresponds closely to the −2 PVU (potential vorticity unit) dynamical tropopause surface (where 1 PVU = 10^6 m^2 s^{-1} K kg^{-1}) [*Alexander et al.*, 2013a]. The radar tropopause is generally ~0.5 km lower than the lapse rate tropopause over these three days in February. Both the radar and lapse rate tropopauses increase about 1 km in altitude until the afternoon of 18 February, before decreasing by a similar amount during the remainder of the observation interval. Large positive and negative vertical velocities of up to 2 m s^{-1} are evident for a 48 h period from

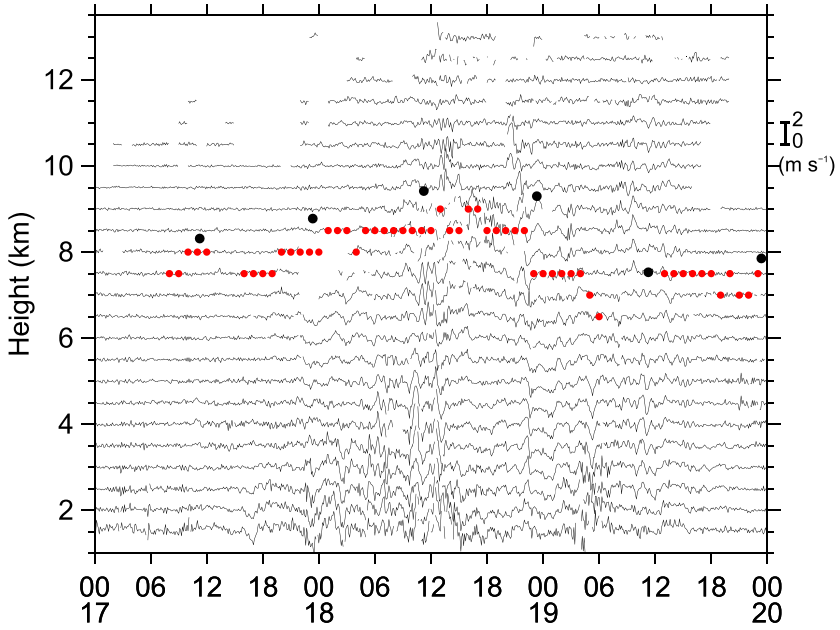

Figure 3. Time-height plot of the vertical wind velocities *w* observed by the VHF radar for 17–19 February. The lapse rate tropopause altitudes calculated from radiosonde data are indicated by the solid black circles and the radar tropopause altitudes by the red circles. The scale is given in the upper right: the length of the bar represents 2 m s^{-1}.

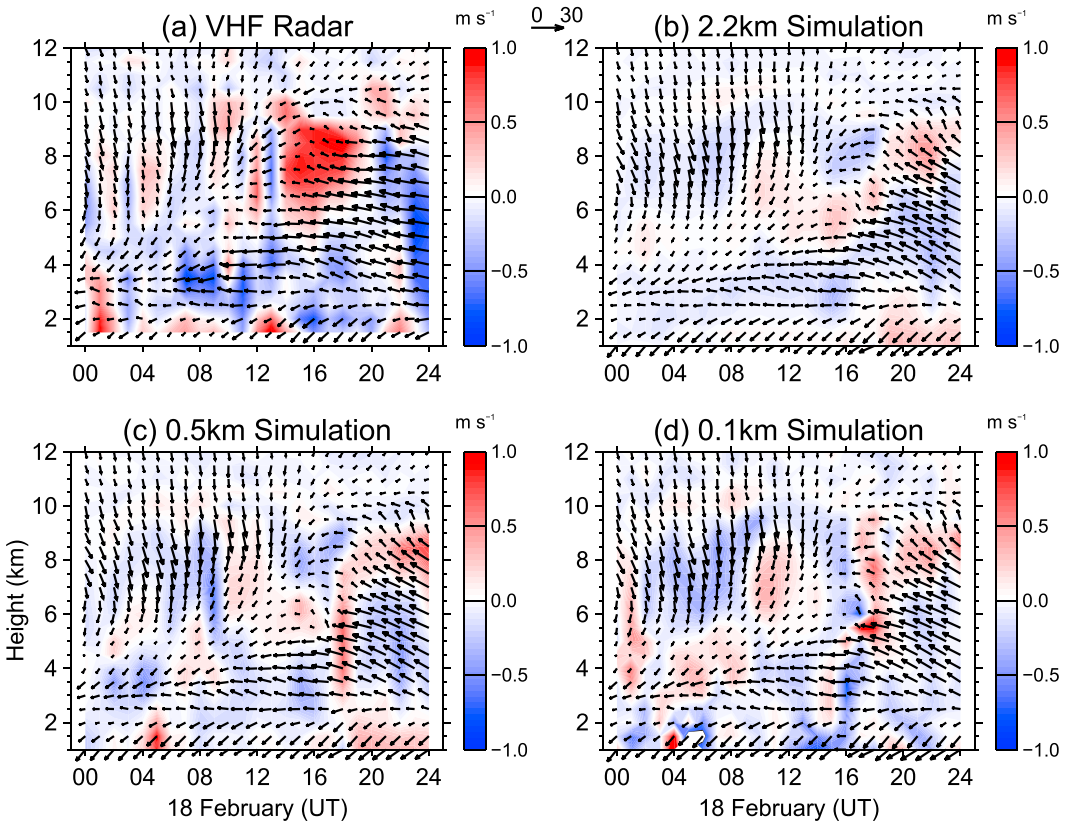

Figure 4. (a) The time-height plot of the hourly averaged 18 February VHF radar horizontal wind field displayed by the vectors (reference vector at the top of the figure, units of m s^{-1}) along with the hourly averaged vertical velocities (color contours). (b–d) The same but for the UM simulations at horizontal grid spacing as indicated in the titles. The horizontal wind vectors are plotted such that for each vector, north is upward and east is to the right.

around 1800 UT 17 February, with the largest amplitudes occurring throughout much of the troposphere between 12 UT and 24 UT 18 February. Out of this period, the vertical winds are damped markedly in the upper troposphere and lower stratosphere.

3.3. Impact of Different Horizontal Grid Spacing on the Simulation of Gravity Waves

The temporal evolution of the hourly averaged vertical profile for both the vertical and horizontal wind components on 18 February observed by VHF radar above Davis is shown in Figure 4a. In the lowest 1–2 km of the troposphere the wind direction is northeasterly throughout much of the day, consistent with the presence of the offshore depression to the north (cf. Figure 2). The horizontal wind field at the beginning of the day varies from easterly in the lower troposphere to northerly in the middle and upper troposphere. The radar measurements indicate hourly averaged vertical wind velocities of up to ± 1 m s^{-1}, with predominantly upward motion in the lower (<2 km altitude) and upper (6–10 km altitude) troposphere, and downward motion in the midtroposphere (3–5 km altitude).

The corresponding horizontal wind fields simulated above Davis on 18 February by the UM are largely insensitive to grid spacing (Figures 4b–4d). All three simulations exhibit a delay in the transition from northerlies to easterlies in the middle and upper troposphere compared with the observations. The simulated vertical velocities show some similarities with the measured vertical winds, although the magnitude of the observed vertical winds are larger and the UM does not always capture the correct phase (which is perhaps due to the delay in the transition from northerlies to easterlies in the middle troposphere compared with the VHF radar observations). The UM simulation fields plotted in Figure 4 are all taken from the closest point to Davis at each horizontal resolution. Choosing other points close to Davis or averaging the four or nine points closest to Davis in the two higher-resolution simulations does not change these results.

The probability distributions of the horizontal wind speeds during 18 February are shown for the VHF radar observations and the UM simulations in Figure 5a. The probability distributions are calculated using the times

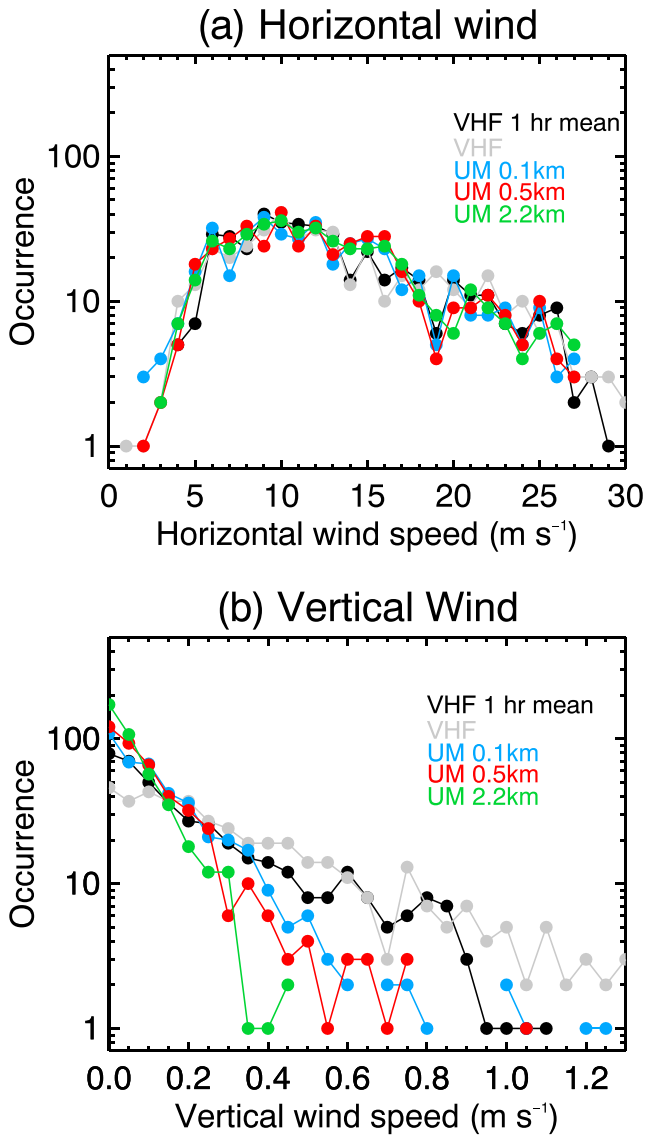

Figure 5. Probability distributions of wind on 18 February 2014 from 1.5 to 12 km altitude, where observational data exist, for the VHF radar along with the three model simulations, as indicated in each panel. (a) Horizontal wind speed; (b) vertical wind speed. The black lines indicate the VHF wind data averaged over the hour, while the grey lines indicate the VHF wind data extracted at the start of each hour.

and altitudes where observations are present. The wind speeds are considered over the 1.5–12 km altitude region, to match the VHF radar's data region. The hourly mean VHF wind data and the VHF wind data extracted at the start of the hour (i.e., 6 min resolution) are indicated. It is clear that all model simulations capture the horizontal wind speed distribution observed by the radar on 18 February. In contrast, the probability distributions of the vertical wind speeds (Figure 5b) indicate that all models, particularly the 2.2 km simulation, underestimate the larger amplitude vertical winds. There is comparatively little difference between the 0.5 km and 0.1 km simulations. This perhaps indicates that the representation of gravity waves in the model has converged by around 0.5 km. However, the vertical velocity amplitudes simulated with the 0.1 km and 0.5 km grid spacing are still below those reported by radar. It is noticeable that the UM fails to reproduce the observed w field completely even using a grid spacing of 0.1 km, which suggests that the model struggles to represent the short-period and small-scale gravity waves which dominate the spectrum at Davis [*Alexander and Murphy*, 2015].

The vertical velocities at an altitude of 1.5 km and 10 m horizontal wind vectors are shown in Figure 6 for 06 UT and 16 UT for each model resolution. These times are selected as they are representative of the two

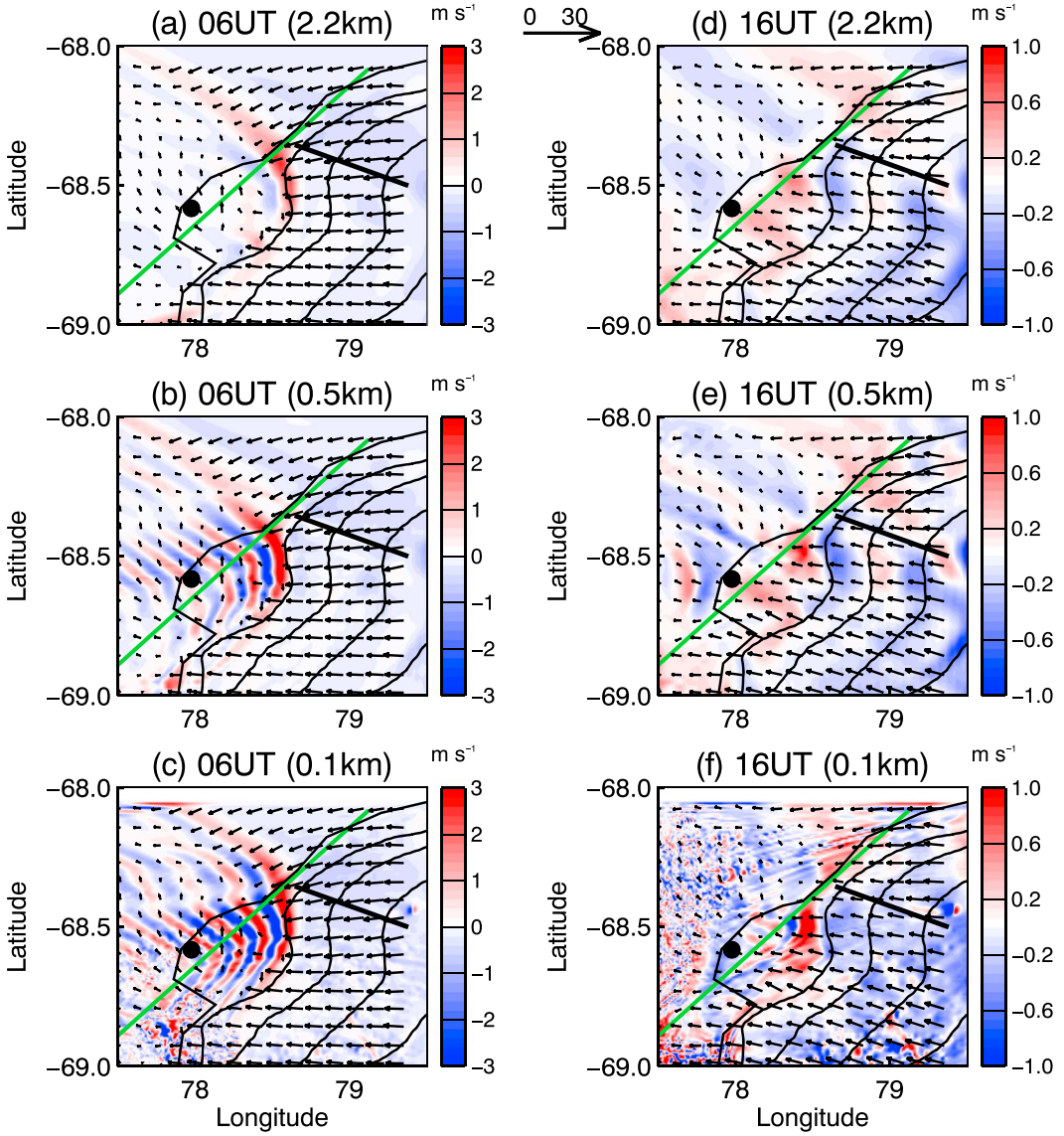

Figure 6. The 1.5 km altitude vertical velocities (color) and 10 m horizontal wind field (vectors) at 06 UT 18 February and 16 UT 18 February for the three horizontal grid spacings: (a, d) 2.2 km, (b, e) 0.5 km, and (c, f) 0.1 km. The horizontal wind field vectors are subsampled for clarity, and its scale is given by the arrow at top center (units of m s^{-1}). Davis is indicated by the black filled circle. The topography is plotted at 500 m intervals. Edge effects north of ~68.2°S in Figures 6c and 6f should be ignored. The green lines indicate the cross sections in Figure 7, and the black lines indicate the location of the ice ridgeline.

distinct regimes in the middle and upper troposphere in the model results, characterized by relatively weak vertical velocities early in the day and stronger vertical velocities later in the day, i.e., at 06 and 16 UT, respectively. All three grid-scale simulations capture the large upward motion at the base of the plateau (centered on 78.5°E, 68.5°S) for both these times. The finer grid scales reveal wave trains at 06 UT extending many horizontal wavelengths westward from the initial phase front at the coastal margin. Larger amplitudes at 06 UT of up to 3 m s^{-1} occur in the 0.1 km grid spacing simulation (the phases are similar in both 0.5 km and 0.1 km simulations) and indicate a horizontal wavelength $\lambda_h \sim 15$ km. A similar pattern of 1.5 km w and strong northeasterly near-surface winds is evident at other times early in the day of 18 February (not shown). The different orientation of the wavefronts and reduced amplitudes at 16 UT are evident. Large-amplitude waves in the lower troposphere at Davis occur in the presence of strong near-surface northeasterly winds above the ice ridgeline [*Alexander and Murphy*, 2015]. The phase lines are broadly oriented perpendicularly to the 10 m wind direction along the coastal margin prior to its interaction with the coastal topography. This is typical

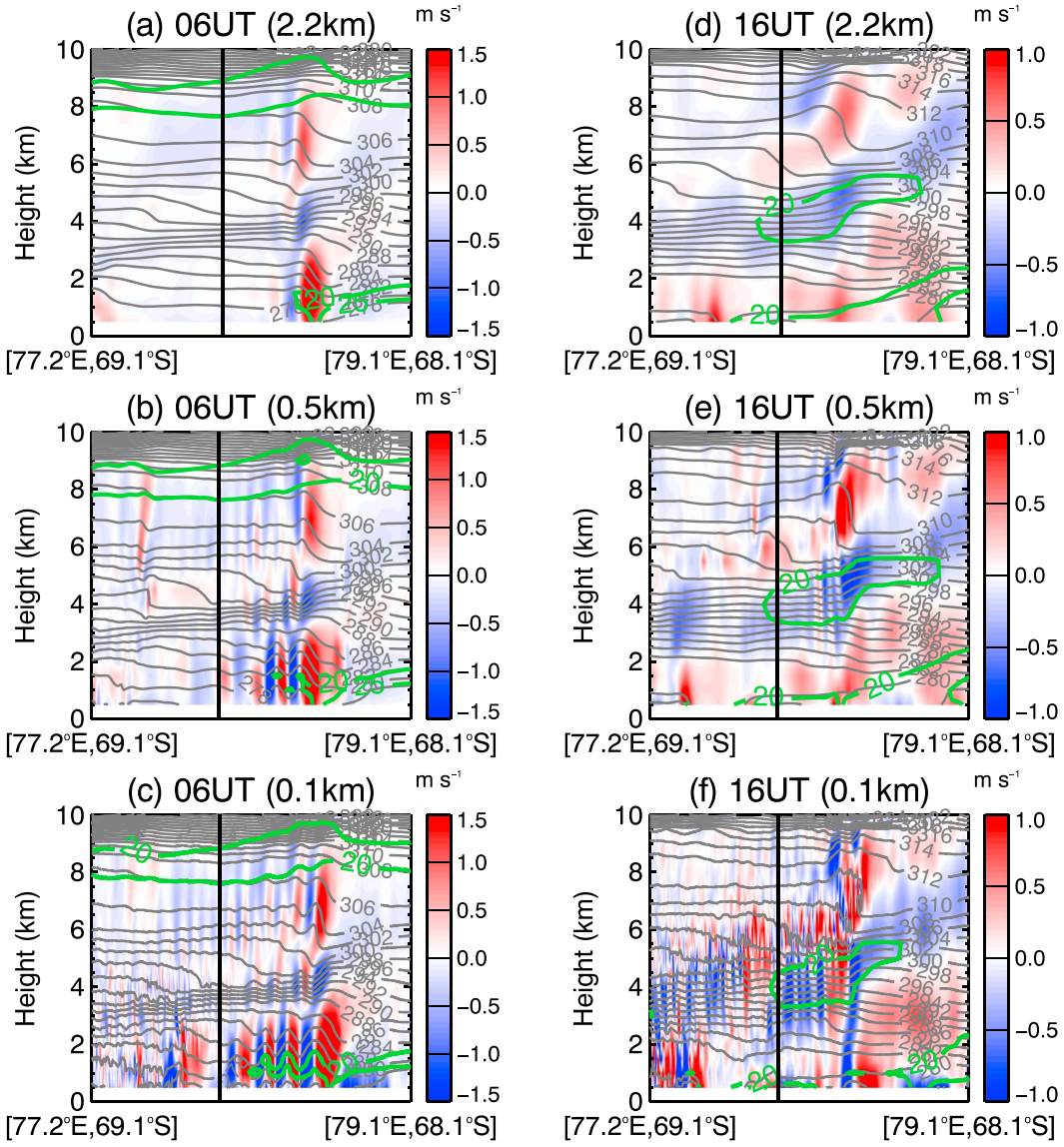

Figure 7. Vertical cross sections of the vertical velocity field (colors), potential temperature (grey lines, units of K), and horizontal wind speed (green lines, units of m s^{-1}, minimum of 20 m s^{-1} displayed) at 06 UT 18 February and 16 UT 18 February for each horizontal grid spacing: (a, d) 2.2 km, (b, e) 0.5 km, and (c, f) 0.1 km. Davis is indicated by the vertical black line in each panel. The cross-section planes are indicated in Figure 6.

of phase fronts associated with katabatic low-level flow passing over orography because of the relationship between the wind and the terrain. Examples of phase fronts whose orientation is more affected by the terrain are present in Figures 6b and 6c southeast of Davis. The weaker wave amplitudes at 16 UT are a result of the changed near-surface horizontal wind field. The 10 m wind field at both times is broadly consistent between the three model simulations. The amplitude of the 10 m winds at 06 UT weaken considerably at Davis as they reach the coastline adjacent to the ice ridgeline and pass over the open ocean. The near-surface flow at 16 UT has changed to easterly or southeasterly over the Antarctic plateau. The offshore winds have veered easterly in the northeasterly edge of the 16 UT plots in Figure 6 and are weak elsewhere. The vertical velocities have weakened markedly, and there is no longer evidence of large-phase fronts around Davis. Nonetheless, a weak pattern of upward and downward motions remain over the sea at 16 UT, although its presence in the 0.1 km resolution simulation is masked somewhat by noise.

Vertical cross sections of the wind field and potential temperature θ are examined in Figure 7 in each of the simulations. The strong horizontal winds flowing down the coastal topography and interacting with

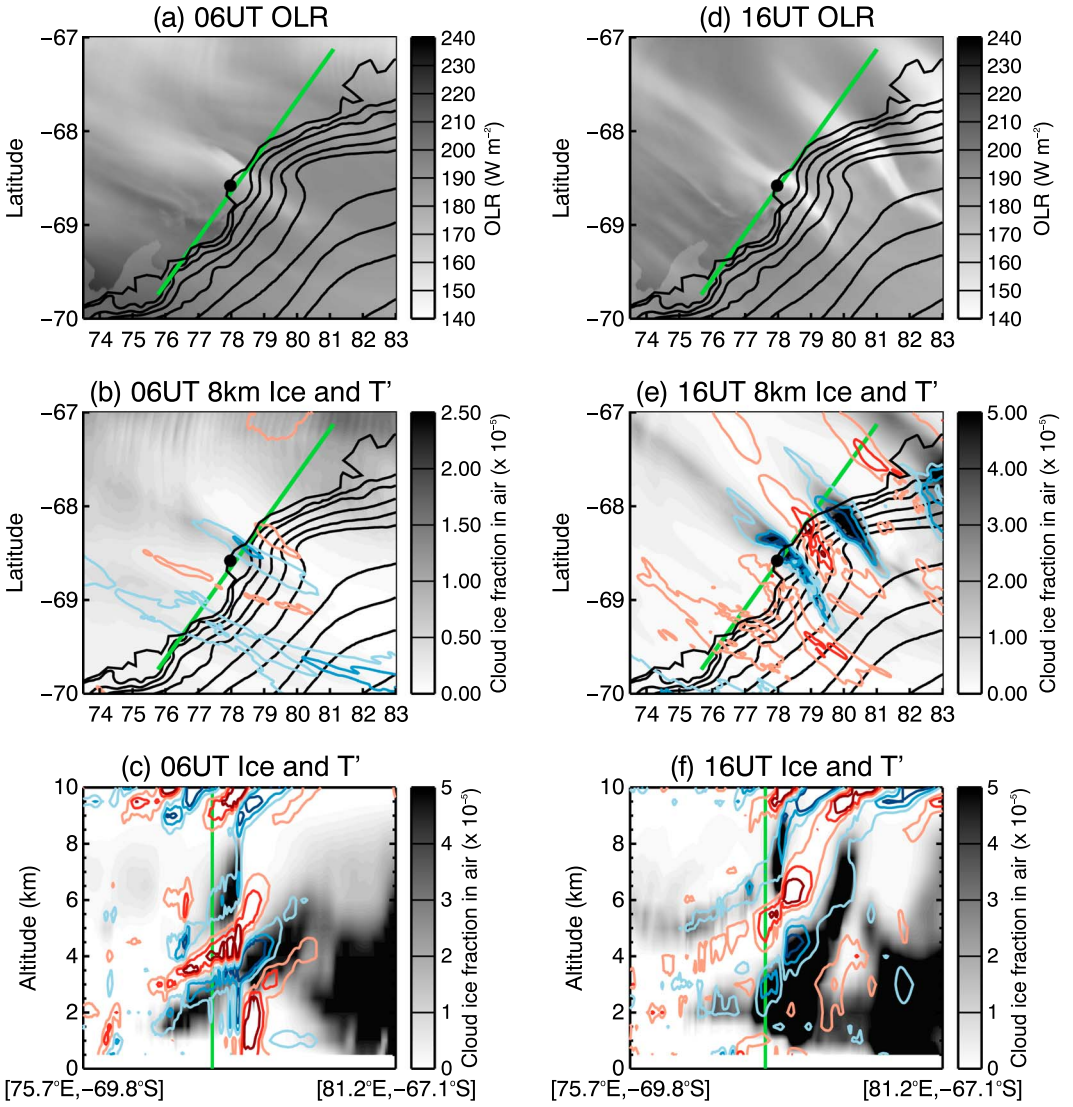

Figure 8. Outgoing longwave radiation field at (a) 06 UT 18 February and (d) 16 UT 18 February from the 0.5 km horizontal grid spacing UM simulation. The 8 km altitude cloud ice fraction in air and small-scale temperature perturbations (positive perturbations: red, negative perturbations: blue, shown at ±0.5, 1.0, and 1.5 K) from the same UM simulation for (b) 06 UT and (e) 16 UT. The green line indicates the vertical cross sections. The vertical cross sections at (c) 06 UT and (f) 16 UT with same temperature perturbations as above. The vertical green line indicates the location of Davis in Figures 8c and 8f.

the offshore winds at 06 UT results in a trapped wave pattern, readily visible in the 0.5 km and 0.1 km simulations. The 2.2 km grid spacing simulation does not capture the trapped nature of these gravity waves, although the location of the waves in the 2.2 km simulation are consistent with the locations in the higher-resolution simulations. Phase changes with altitude are clearly visible in all simulations, indicating a vertical wavelength $\lambda_z \sim 5$ km. The largest amplitudes of these gravity waves are trapped due to (at least partial) reflection at a stable layer present at about 3.5 km altitude [*Wells and Vosper*, 2010]. The sensitivity of the results to horizontal resolution is different at 06 UT than it is at 16 UT. The higher-resolution simulations add wavelengths to the trapped wave in the lower troposphere but leave the signal little changed at the coast. In contrast, small-scale motions are evident at higher resolutions at 16 UT which suggests turbulent motions. The wavelength in the upper troposphere decreases for increased horizontal resolutions at this time.

The 06 UT vertical profiles presented in Figure 7 are indicative of wave trapping in the lower troposphere. The wave phases of *w* at 16 UT are tilted with altitude into the direction of the prevailing surface wind and indicates that the waves direct wave energy upward and against the propagation direction of the surface wind.

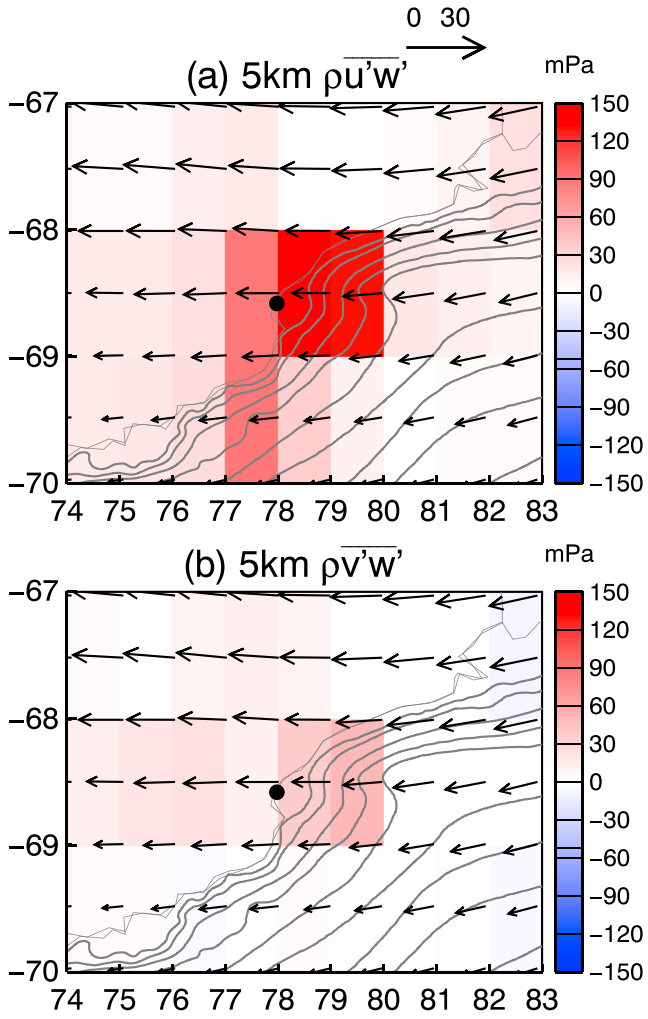

Figure 9. Gravity wave momentum fluxes calculated using the 0.5 km horizontal grid cell UM simulation at 5 km altitude. The fluxes are averaged over 18 February into 1° × 1° grid cells. (a) The zonal component of the flux and (b) the meridional component of the flux. The vectors indicate the daily mean horizontal wind field at 5 km altitude, with scale given at top (units of m s^{-1}). Davis is indicated by the solid black circle.

Such behavior is a characteristic of an orographic source for these gravity waves [*Plougonven et al.*, 2008]. Indeed, orographic gravity wave activity has previously been reported along the east Antarctic coastline during the passage of offshore cyclones [*Alexander and Murphy*, 2015; *Tomikawa et al.*, 2015].

3.4. Clouds Above Davis

A close inspection of Figure 2 reveals the presence of high cloud tops (indicated by the low IR brightness temperature) above Davis. To investigate the possibility that these clouds above Davis are being forced by the waves evident in radar observations and the UM simulations during the 18 February 2014 event, we examine the cloud distribution from UM outputs in detail. While small horizontal scale fluctuations dominate the vertical velocity field (not shown), the temperature and horizontal wind fields are dominated by synoptic-scale motions. In order to isolate the temperature perturbations T' of the orographic gravity waves associated with clouds, temperatures with horizontal scales less than 250 km are extracted from the background field. This 250 km horizontal limit is chosen for consistency with the limit used to extract wind velocity perturbation fields in the model for the momentum flux calculations below. It allows retention of the waves which likely influence small-scale cloud formation or dissipation and is based upon an inspection of the model wind, ice cloud, and temperature fields.

The outgoing longwave radation (OLR) simulated by the UM at 0.5 km grid spacing is shown in Figure 8 for 06 UT and 16 UT. Lower OLR values indicate higher-level cloud. The model indicates the presence of high cloud

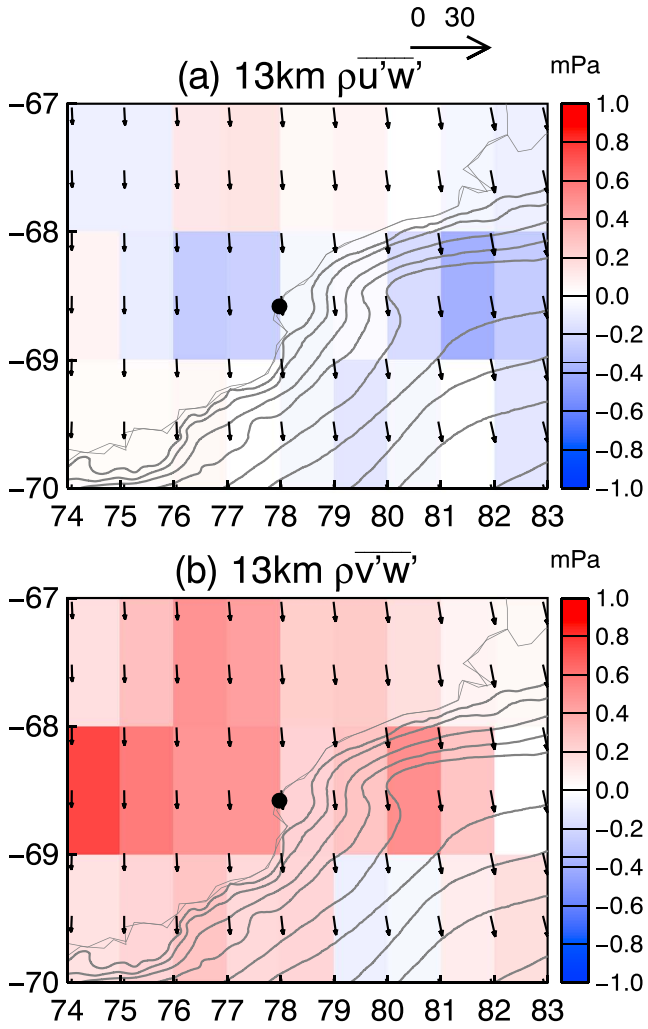

Figure 10. As for Figure 9 but at 13 km altitude. Note the much smaller color scales here than in Figure 9.

extending out over the sea to the northwest of Davis at both these times, which is consistent with satellite observations of cloud presence (Figure 2). The cloud ice fraction in air at 8 km is illustrated in Figures 8b and 8e. Regions of relatively high cloud ice fraction in air coincide with the cold phases of small-scale waves, that is, localized cooling due to adiabatic temperature changes induced by upward moving air parcels. On the other hand, the cloud ice fraction further northeast and offshore (upstream) of Davis at 06 UT is unrelated to the phase of T' and instead is likely present due to synoptic-scale processes. The 8 km altitude temperature perturbations at both 06 UT and 16 UT are oriented similarly. The results from the simulations at 2.2 km and 0.1 km horizontal grid spacing (not shown) were broadly similar to the 0.5 km results, with both also able to capture the temperature perturbations responsible for ice cloud formation directly upstream of Davis.

Vertical cross sections of cloud ice fraction at both times are shown in Figures 8c and 8f. The cross sections are from the same transect as the vertical velocity transects of Figure 7 and are oriented approximately perpendicular to the gravity wave phase fronts at 8 km. The effect of the temperature perturbations of amplitude up to 1.5 K, induced by the orographic gravity waves, is clear. Throughout the troposphere around Davis, cloud ice fraction increases in the cold phases of these waves and decreases (or is absent) in the warm phases. The 06 UT cross section indicates the synoptic nature of the ice cloud northeast of Davis (to the right in this subfigure), where large cloud ice fraction is present throughout the lower and middle troposphere but not related to small-scale T'. Due to the trapped nature of the 06 UT waves, the large T' (Figure 8c) are confined to the lower to middle troposphere and directly upstream (to the right) of Davis, as well as being vertically orientated.

3.5. Gravity Wave Momentum Fluxes

To quantify the impact of the orographic gravity waves on the atmosphere, the zonal and meridional components of vertical momentum flux (MF) are calculated. The wind velocity perturbations must be extracted by selection of an appropriate background. We follow the approach of *Plougonven et al.* [2013] in their analysis of WRF model simulations over the Southern Hemisphere and isolate the small-scale part of the flow using a moving average. Wind velocities with horizontal scales less than 250 km are retained for this analysis. This limit is chosen based on the horizontal scales of the observed velocity perturbation fields. To provide a large set of data values in order to reduce uncertainties in the MF calculations, the zonal and meridional MF $\rho\overline{u'w'}$ and $\rho\overline{v'w'}$ are averaged spatially and temporally over the whole day and into a grid with dimension $1° \times 1°$.

The daily MF at 5 km and 13 km are shown in Figures 9 and 10, respectively, binned into $1° \times 1°$ grid cells. In the midtroposphere, discrete, localized coastal regions of large positive (eastward flux) $\rho\overline{u'w'}$ are evident, especially around Davis. The waves are propagating against the dominant westward flow at 5 km. The equivalent plot of the weaker meridional MF indicates mostly positive (northward) flux over the coast. Together, the large positive $\rho\overline{u'w'}$ and $\rho\overline{v'w'}$ along the coastline are indicative of orographic waves occurring in a northeasterly background flow.

The tropospheric fluxes are large with absolute MF peaking locally around 150 mPa. In contrast, the MF in the lower stratosphere are negligible and generally <1 mPa. These negligibile lower stratospheric MF (compare with other modeling and observational reports of events in the tens of mPa [*Plougonven et al.*, 2015; *Vosper*, 2015]) indicate the absorption into the background flow of orographic gravity waves generated on this day. The resultant accelerations in the upper troposphere are negligible compared with other processes which vary the wind in this region. We note that instrumental limitations using the VHF radar prohibits its ability to compute momentum fluxes.

4. Discussion

The UM simulations reveal the orographic origin of the vertical velocity fluctuations evident in the VHF radar data during 18 February 2014. The simulations indicate that small-scale temperature perturbations T' of up to 1.5 K influence the location of ice cloud above and in the vicinity of Davis throughout the troposphere. Localized cooling due to adiabatic temperature changes induced by upward moving air parcels results in the formation of ice cloud, whereas regions of downward moving air parcels result either in reduced cloud ice fraction or in its absence altogether. The trapped orographic gravity waves, present during the early part of 18 February, are oriented in the direction of the background flow incident upon the obstacle (i.e., a little north of easterly) and are absorbed into the background around the tropopause, where the flow is northerly. The projection of these wind fields onto the gravity wave propagation direction reverses sign, resulting in (partial) critical-level absorption and a consequent reduction in wave amplitude [*Xu et al.*, 2012]. By the end of the day the horizontal wind field in the middle to upper troposphere is easterly, which coincides with relatively reduced absorption and therefore larger vertical velocities reaching the tropopause. In contrast to the summer case study presented here, orographic gravity waves in Antarctica do propagate into the stratosphere under favorable background wind conditions. In particular, a combination of observations and modeling studies have demonstrated that orographic gravity waves form Antarctic polar stratospheric clouds during winter under favorable wind conditions and when the background temperature is close to their formation threshold [e.g., *Höpfner et al.*, 2006; *Noel et al.*, 2008; *Eckermann et al.*, 2009; *Noel et al.*, 2009; *Alexander et al.*, 2013b; *Orr et al.*, 2015]. These stratospheric clouds are formed in the same way as the cirrus clouds at Davis, that is, by local cooling induced by the upwardly moving air parcels.

Locally, above Davis, all UM simulations (0.1 km, 0.5 km, and 2.2 km horizontal grid spacing) captured the orographic gravity waves formed on the downslope side of an ice ridgeline some 60 km northeast of Davis at 06 UT (Figure 6), formed due to the interactions between the synoptic offshore cyclonic winds, katabatic winds, and the coastal topography. The temporal evolution of the horizontal wind fields above Davis simulated by the UM is largely independent of the horizontal grid spacing. The representation of gravity waves in the model, manifested as large vertical velocities, has converged by around 0.5 km. Both the 0.1 km and 0.5 km resolution simulations at 06 UT indicated that the wave trains extended westward out to sea. The vertical cross sections at this time indicated wave trapping inhibiting the waves propagating freely into the stratosphere. In contrast, the 16 UT vertical cross sections revealed that a changed background atmosphere and the tilting of the waves' phase fronts into the direction of the wind is evident. The waves during the latter half

of 18 February are not trapped and are of smaller amplitude. As part of a study on convectively generated gravity waves, *Lane and Knievel* [2005] found that higher horizontal resolution simulations increased the likelihood of vertically trapped waves, which propagated upward freely at coarser resolutions. This can also be seen in Figure 7 for the orographic gravity wave, which shows evidence of trapping in the higher-resolution simulations at 06 UT. Nonetheless, for this case, large-amplitude fluctuations remain visible in the upper troposphere for all simulations directly above the base of the plateau. Orographic wave properties are also sensitive to horizontal resolution of model simulations. *Smith et al.* [2006] showed that surface pressure drag increases in the Alps as horizontal resolution decreases.

Winds associated with cyclones centered over the ocean interact with the coastal topography and katabatic winds which results in orographic wave production along the East Antarctic coast [*Turner et al.*, 2009; *Orr et al.*, 2014]. Smaller cyclones are particularly prominent around East Antarctica [*Irving et al.*, 2010] but are poorly resolved by coarse-resolution global climate models, which have grid spacing of the order 100–200 km [*Ohfuchi et al.*, 2004; *Condron and Renfrew*, 2013]. The coarse resolution of these models additionally results in an underrepresentation of local topographic variations, such as along the coastal margins, resulting in a generally poor representation of katabatic winds in this region [*Bintanja et al.*, 2014]. Yet the interaction of the katabatic wind with winds from offshore cyclones drives orographic gravity wave production. The presence and passage of Southern Ocean cyclones is a common occurrence throughout the year, although the seasonal cycle of their horizontal and vertical velocity variances in the lower troposphere indicates a peak in winter [*Alexander and Murphy*, 2015]. Orographic-related cloud forcing by these cyclones along coastal East Antarctica is not limited to this one case study examined here. Although not discussed in their text, these wave clouds are also clearly visible in satellite and simulation results of a wintertime cyclone passing north of Syowa station [*Tomikawa et al.*, 2015].

5. Conclusion

Unique, high-resolution simulations by the UM on 18 February 2014 were performed to understand the large vertical velocities observed by a VHF radar at Davis, Antarctica (69°S, 78°E), and place the radar's observations into a regional context. Three UM simulations with horizontal grid spacing of 0.1 km, 0.5 km, and 2.2 km were performed. The temporal evolution of the UM simulations' horizontal wind fields above Davis are largely independent of grid spacing. All simulations indicated that orographic gravity waves formed due to the interaction of the offshore synoptic flow with the coastal topography. As the background horizontal wind field changed throughout the day, the waves' properties varied. At 06 UT, a trapped wave was identified, while at 16 UT, the wavefield around Davis had altered and the classic pattern of orographic gravity waves with phases tilted into the prevailing wind direction was present.

The observed and modeled orographic waves disappeared by the lower stratosphere due to critical-level absorption as the wind direction changed from low-level easterlies to northerlies in the lower stratosphere. This resulted in negligible lower stratospheric momentum fluxes, compared with strong northeastward momentum flux present in the midtroposphere, opposing the direction of the background flow. Ice cloud simulated by the UM above Davis were present in the cool phases of small-scale waves which adiabatically cooled the local environment.

The UM simulations were able to resolve the enhanced vertical velocities which were also present in the VHF radar data, although the amplitude of the vertical velocities remained underestimated by the model at all resolutions. The probability distributions of vertical velocities was similar for both the 0.5 km and 0.1 km simulations, indicating convergence of the gravity waves present in the model by 0.5 km. By combining new ground-based Antarctic observations with high-resolution numerical modeling, case studies such as this one help illuminate and quantify the role that synoptic-scale weather systems have in producing orographic gravity waves and ice clouds along the East Antarctic coastline. In particular, the crucial role these waves have in forming ice clouds and producing large vertical momentum fluxes was identified in this summertime case study. High-resolution simulations such as this one should be exploited to quantify and improve the representation in global climate models of localized atmospheric processes.

Appendix A: Validation of the Radar's Horizontal Wind Velocities

Winds derived from radar observations are compared against colocated radiosonde data to validate the former. This is illustrated for the upgraded Davis VHF radar for the period February 2014 to February 2016

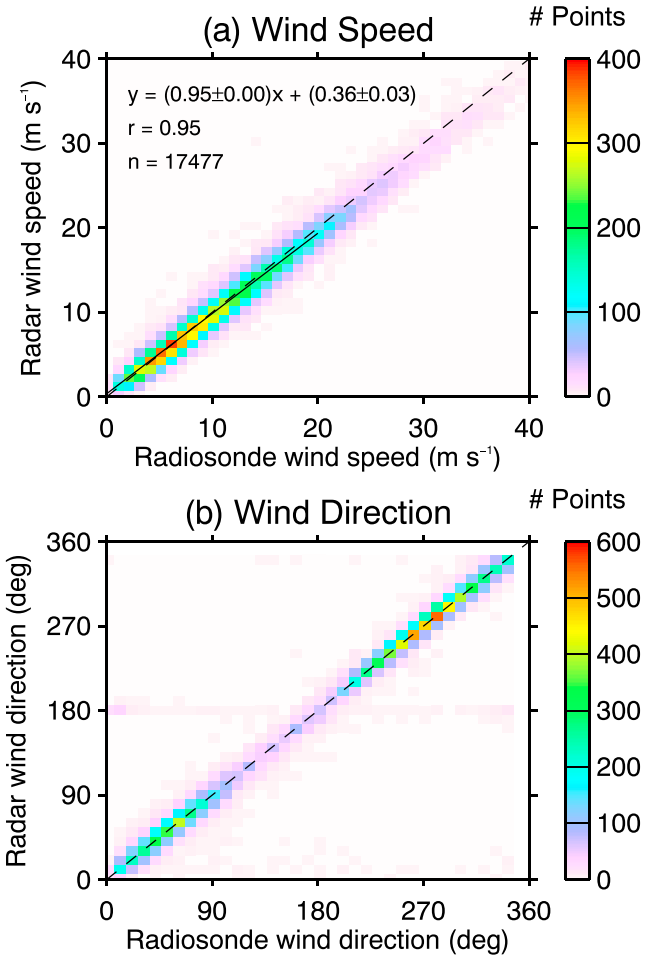

Figure A1. The comparison between radiosonde and radar winds for February 2014 to February 2016 inclusive for (a) wind speed and (b) wind direction. Radar data are averaged within an hour of the radiosonde launch times. The linear fit parameters, correlation, and number of data points are detailed in Figure A1a. The dashed lines indicate the 1:1 fit, and the solid line in Figure A1a is the linear fit.

inclusive in Figure A1. Hourly quality-controlled radar wind profiles [*Dolman and Reid*, 2014] are extracted when they coincide with a colocated radiosonde launch, for all altitudes where the radar's signal-to-noise ratio > -12 dB. These results are a marked improvement over the radar's results prior to the change to Doppler-only operation (see the lower tropospheric only results in *Alexander and Murphy* [2015, Figure 3]). Specifically, the linear regression gradient is now 0.95 (0.76 previously) and $r = 0.95$ ($r = 0.93$ previously). Compared with the original system, the wind directions still agree closely between radar and radiosonde, with only a few isolated outlying points.

Acknowledgments
We thank the Davis engineers for their efforts upgrading and maintaining the VHF wind-profiling radar and the Bureau of Meteorology staff who launched the radiosondes. The UM simulations were run at the UK Met Office. The UM simulation data, the VHF radar data, and the radiosonde data are available from the authors upon request. ERA-Interim data were downloaded from the ECMWF server, and the NOAA satellite data were downloaded from the NOAA Comprehensive Large Array-data Stewardship System (CLASS) server after registration. We thank Tony Phillips at BAS for producing Figure 1. This research was conducted for projects 4025 and 4292 of the Australian Antarctic program. and funded by the Australian Antarctic Division, Department of the Environment, Australia (10.13039/501100005108).

References

Alexander, S. P., and D. J. Murphy (2015), The seasonal cycle of lower-tropospheric gravity wave activity at Davis, Antarctica (69°S, 78°E), *J. Atmos. Sci.*, *72*, 1010–1021, doi:10.1175/JAS-D-14-0171.1.

Alexander, S. P., A. R. Klekociuk, M. C. Pitts, A. J. McDonald, and A. Arevalo-Torres (2011), The effect of orographic gravity waves on Antarctic polar stratospheric cloud occurrence and composition, *J. Geophys. Res.*, *116*, D06109, doi:10.1029/2010JD015184.

Alexander, S. P., D. J. Murphy, and A. R. Klekociuk (2013a), High resolution VHF radar measurements of tropopause structure and variability at Davis, Antarctica (69°S, 78°E), *Atmos. Chem. Phys.*, *13*, 3121–3132, doi:10.5194/acp-13-3121-2013.

Alexander, S. P., A. R. Klekociuk, A. J. McDonald, and M. C. Pitts (2013b), Quantifying the role of orographic gravity waves on polar stratospheric cloud occurrence in the Antarctic and the Arctic, *J. Geophys. Res. Atmos.*, *118*, 11,493–11,507, doi:10.1002/2013JD020122.

Alexander, S. P., K. Sato, S. Watanabe, Y. Kawatani, and D. J. Murphy (2016), Southern Hemisphere extra-tropical gravity wave sources and intermittency revealed by a middle-atmosphere general circulation model, *J. Atmos. Sci.*, *73*, 1335–1349, doi:10.1175/JAS-D-15-0149.1.

Arnault, J., and S. Kirkwood (2012), Dynamical influence of gravity waves generated by the Vestfjella Mountains in Antarctica: Radar observations, fine-scale modelling and kinetic energy budget analysis, *Tellus A*, *64*, 17261, doi:10.3402/tellusa.v64i0.17261.

Bintanja, R., C. Severijns, R. Haarsma, and W. Hazelege (2014), The future of Antarctica's surface winds simulated by a high-resolution global climate model, *J. Geophys. Res. Atmos.*, *119*, 7136–7159, doi:10.1002/jgrd.v.119.12.

Condron, A., and I. A. Renfrew (2013), The impact of polar mesoscale storms on northeast Atlantic Ocean circulation, *Nat. Geosci.*, *6*, 34–37, doi:10.1038/ngeo1661.
Davies, T., M. J. P. Cullen, A. J. Malcolm, M. H. Mawson, A. Stainforth, A. A. White, and N. Wood (2005), A new dynamical core for the MetOffice's global and regional modelling of the atmosphere, *Q. J. R. Meteorol. Soc.*, *131*, 1759–1782, doi:10.1256/qj.04.101.
Dean, S., B. Lawrence, R. Grainger, and D. Heuff (2005), Orographic cloud in a GCM: The missing cirrus, *Clim. Dyn.*, *24*, 771–780.
Dee, D. P., et al. (2011), The ERA-Interim reanalysis: Configuration and performance of the data assimilation system, *Q. J. R. Meteorol. Soc.*, *137*, 553–597, doi:10.1002/qj.828.
Dolman, B. K., and I. M. Reid (2014), Bias correction and overall performance of a VHF Spaced Antenna boundary layer profiler for operational weather forecasting, *J. Atmos. Sol. Terr. Phys.*, *118*, 16–24, doi:10.1016/j.jastp.2014.02.009.
Eckermann, S. D., L. Hoffmann, M. Höpfner, D. L. Wu, and M. J. Alexander (2009), Antarctic NAT PSC belt of June 2003: Observational validation of the mountain wave seeding hypothesis, *Geophys. Res. Lett.*, *36*, L02807, doi:10.1029/2008GL036629.
Gage, K. S., and J. L. Green (1979), Tropopause detection by partial specular reflection with very high frequency radar, *Science*, *203*, 1238–1240.
Guest, F. M., M. J. Reeder, C. J. Marks, and D. J. Karoly (2000), Inertia-gravity waves observed in the lower stratosphere over Macquarie Island, *J. Atmos. Sci.*, *57*, 737–752.
Hendricks, E. A., J. D. Doyle, S. D. Eckermann, Q. Jiang, and P. A. Reinecke (2014), What is the source of the stratospheric gravity wave belt in austral winter?, *J. Atmos. Sci.*, *71*, 1583–1592, doi:10.1175/JAS-D-13-0332.1.
Hoffmann, L., X. Xue, and M. J. Alexander (2013), A global view of stratospheric gravity wave hotspots located with Atmospheric Infrared Sounder observations, *J. Geophys. Res. Atmos.*, *118*, 416–434, doi:10.1029/2012JD018658.
Höpfner, M., et al. (2006), MIPAS detects Antarctic stratospheric belt of NAT PSCs caused by mountain waves, *Atmos. Chem. Phys.*, *6*, 1221–1230.
Hunt, J. C. R., A. Orr, J. W. Rottman, and R. Capon (2004), Coriolis effects in mesoscale flows with sharp changes in surface conditions, *Q. J. R. Meteorol. Soc.*, *130*, 2703–2731, doi:10.1256/qj.04.14.
Irving, D., I. Simmonds, and K. Keay (2010), Mesoscale cyclone activity over the ice-free Southern Ocean: 1999–2008, *J. Clim.*, *23*, 5404–5420, doi:10.1175/2010JCLI3628.1.
Kärcher, B., and J. Ström (2003), The roles of dynamical variability and aerosols in cirrus cloud formation, *Atmos. Chem. Phys.*, *3*, 823–838.
Lane, T. P., and J. C. Knievel (2005), Some effects of model resolution on simulated gravity waves generated by deep, mesoscale convection, *J. Atmos. Sci.*, *62*, 3408–3419.
Ludlam, F. H. (1952), Orographic cirrus clouds, *Q. J. R. Meteorol. Soc.*, *78*, 552–562.
Nigro, M. A., J. J. Cassano, M. A. Lazzara, and L. M. Keller (2012), Case study of a barrier wind corner jet off the coast of the Prince Olaf Mountains, Antarctica, *Mon. Weather Rev.*, *140*, 2044–2063, doi:10.1175/MWR-D-11-00261.1.
Noel, V., A. Hertzog, H. Chepfer, and D. M. Winker (2008), Polar stratospheric clouds over Antarctica from the CALIPSO spaceborne lidar, *J. Geophys. Res.*, *113*, D02205, doi:10.1029/2007JD008616.
Noel, V., A. Hertzog, and H. Chepfer (2009), CALIPSO observations of wave-induced PSCs with near-unity optical depth over Antarctica in 2006–2007, *J. Geophys. Res.*, *114*, D05202, doi:10.1029/2008JD010604.
Ohfuchi, W., et al. (2004), 10 km mesh mesoscale resolving simulations of the global atmosphere on the Earth Simulator, *J. Earth Sim.*, *1*, 8–34.
Orr, A., D. Cresswell, G. J. Marshall, J. C. R. Hunt, J. Sommeria, C. G. Wang, and M. Light (2004), A 'low-level' explanation for the recent large warming trend over the western Antarctic Peninsula involving blocked winds and changes in zonal circulation, *Geophys. Res. Lett.*, *31*, L06204, doi:10.1029/2003GL019160.
Orr, A., J. C. R. Hunt, R. Capon, J. Sommeria, D. Cresswell, and D. Owinoh (2005), Coriolis effects on wind jets and cloudiness along coasts, *Weather*, *60*, 291–299, doi:10.1256/wea.219.04.
Orr, A., R. Phillips, S. Webster, A. Elvidge, M. Weeks, J. S. Hosking, and J. Turner (2014), Met Office Unified Model high resolution simulations of a strong wind event in Antarctica, *Q. J. R. Meteorol. Soc.*, *140*, 2287–2297, doi:10.1002/qj.2296.
Orr, A., J. S. Hosking, L. Hoffmann, J. Keeble, S. M. Dean, H. K. Roscoe, N. L. Abrahams, S. Vosper, and P. Braesicke (2015), Inclusion of mountain-wave-induced cooling for the formation of PSCs over the Antarctic Peninsula in a chemistry-climate model, *Atmos. Chem. Phys.*, *15*, 1071–1086, doi:10.5194/acp-15-1071-2015.
Owinoh, A., J. C. R. Hunt, A. Orr, P. Clark, R. Klein, H. J. S. Fernando, and F. T. N. Nieuwstadt (2005), Effects of changing surface heat flux on the atmospheric boundary layer over flat terrain, *Boundary Layer Met.*, *116*, 331–361, doi:10.1007/s10546-004-2819-z.
Petersen, G. N., I. A. Renfrew, and G. W. K. Moore (2009), An overview of barrier winds off southeastern Greenland during the Greenland Flow Distortion experiment, *Q. J. R. Meteorol. Soc.*, *135*, 1950–1967, doi:10.1002/qj.455.
Plougonven, R., A. Hertzog, and H. Teitelbaum (2008), Observations and simulations of a large amplitude mountain wave breaking over the Antarctic Peninsula, *J. Geophys. Res.*, *113*, D16113, doi:10.1029/2007JD009739.
Plougonven, R., A. Hertzog, and L. Guez (2013), Gravity waves over Antarctica and the Southern Ocean: Consistent momentum fluxes in mesoscale simulations and stratospheric balloon observations, *Q. J. R. Meteorol. Soc.*, *139*, 101–118, doi:10.1002/qj.1965.
Plougonven, R., A. Hertzog, and M. J. Alexander (2015), Case studies of non-orographic gravity waves over the Southern Ocean emphasize the role of moisture, *J. Geophys. Res. Atmos.*, *120*, 1278–1299, doi:10.1002/2014JD022332.
Sato, K., S. Tateno, S. Watanabe, and Y. Kawatani (2012), Gravity wave characteristics in the Southern Hemisphere revealed by a high-resolution middle-atmosphere general circulation model, *J. Atmos. Sci.*, *69*, 1378–1396, doi:10.1175/JAS-D-11-0101.1.
Smith, R. B. (1979), The influence of mountains on the atmosphere, *Adv. Geophys.*, *21*, 187–230.
Smith, S. A., J. D. Doyle, A. R. Brown, and S. Webster (2006), Sensitivity of resolved mountain drag to model resolution for MAP case-studies, *Q. J. R. Meteorol. Soc.*, *132*, 1467–1487.
Steinhoff, D. F., D. H. Bromwich, M. Lambertson, S. L. Knuth, and M. A. Lazzara (2008), A dynamical investigation of the May 2004 McMurdo Antarctica severe wind event using AMPS, *Mon. Weather Rev.*, *136*, 7–26, doi:10.1175/2007MWR1999.1.
Stephens, G. L. (2002), *Cirrus*, pp. 433–448, chap. Cirrus, climate, and global change, edited by D. K. Lynch et al., Oxford Univ. Press, Oxford, U. K.
Tomikawa, Y., M. Nomoto, H. Miura, M. Tsutsumi, K. Nishimura, T. Nakamura, H. Yamagishi, T. Yamanouchi, T. Sato, and K. Sato (2015), Vertical wind disturbances during a strong wind event observed by the PANSY radar at Syowa Station, Antarctica, *Mon. Weather Rev.*, *143*, 1804–1821, doi:10.1175/MWR-D-14-00298.1.
Turner, J., S. N. Chenoli, A. A. Samah, G. Marshall, T. Phillips, and A. Orr (2009), Strong wind events in the Antarctic, *J. Geophys. Res.*, *114*, D18103, doi:10.1029/2008JD011642.
Valkonen, T., T. Vihma, S. Kirkwood, and M. Johansson (2010), Fine-scale modelling simulation of gravity waves generated by Basen nunatak in Antarctica, *Tellus*, *62A*, 319–332.

Vosper, S. B. (2015), Mountain waves and wakes generated by South Georgia: Implications for drag parameterization, *Q. J. R. Meteorol. Soc.*, *141*, 2813–2827, doi:10.1002/qj.2566.

Watanabe, S., K. Sato, and M. Takahashi (2006), A general circulation model study of the orographic gravity waves over Antarctica excited by katabatic winds, *J. Geophys. Res.*, *111*, D18104, doi:10.1029/2005JD006851.

Wells, H., and S. B. Vosper (2010), The accuracy of linear theory for predicting momentum drag: Implications for parameterization schemes, *Q. J. R. Meteorol. Soc.*, *136*, 429–441.

Xu, X., Y. Wang, and M. Xue (2012), Momentum flux and flux divergence of gravity waves in directional shear flows over three-dimensional mountains, *J. Atmos. Sci.*, *69*, 3733–3744.